Geochemistry, Geophysics, Geosystems®

Key Points:

- We present a data set of dissolved stable Ba isotopic compositions in surface sediment pore waters of a large river estuary
- Pore water Ba isotope values generally decrease with increasing sediment depth, reflecting post-depositional Ba isotope fractionation
- A diffusion-reaction model predicts the distribution and fractionation of stable Ba isotopes in the sediment pore waters well
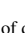
Stable Barium Isotope Fractionation in Pore Waters of Estuarine Sediments

Zhimian Cao[1] ®, Xinting Rao[1], Yating Li[1], Qingquan Hong[1] ®, Lin Wei[1], Yang Yu[2] ®, Claudia Ehlert[3], Bo Liu[4] ®, Christopher Siebert[2], Ed C. Hathorne[2] ®, Zhouling Zhang[2] ®, Florian Scholz[2], Sabine Kasten[4,5], and Martin Frank[2]

[1]State Key Laboratory of Marine Environmental Science, College of Ocean and Earth Sciences, Xiamen University, Xiamen, China, [2]GEOMAR Helmholtz Center for Ocean Research Kiel, Kiel, Germany, [3]Institute for Chemistry and Biology of the Marine Environment, University of Oldenburg, Oldenburg, Germany, [4]Alfred Wegener Institute Helmholtz Centre for Polar and Marine Research, Bremerhaven, Germany, [5]Faculty of Geosciences, University of Bremen, Bremen, Germany

Abstract The development of stable barium (Ba) isotope measurements provides a novel tool to investigate the geochemical cycling of Ba in the ocean and its sediments. In sediment pore waters, gradients of dissolved Ba concentrations result from various diagenetic processes. The distribution and fractionation of Ba isotopes in the pore waters are expected to further improve our understanding of these early diagenetic control mechanisms. Here, we present pore water profiles of dissolved stable Ba isotopic signatures ($\delta^{138}Ba_{pw}$) from shallow water sediments covering the entire Pearl River Estuary (PRE) in Southern China. We find pronounced depth-dependent Ba isotope variations generally showing a shift from heavy to light $\delta^{138}Ba_{pw}$ signatures from the sediment surface down to 15 cm depth. These gradients are well reproduced by a diffusion-reaction model, which generates an apparent fractionation factor ($^{138}\varepsilon$) of $-0.60 \pm 0.10‰$ pointing to preferential removal of low-mass Ba isotopes from the pore water during solution-solid phase interactions. Consequently, the combined diagenetic processes induce the highest $\delta^{138}Ba_{pw}$ values of $+0.5$ to $+0.7‰$ in the pore waters of the topmost sediment layer. Although the detrital fraction dominates the Ba content in the PRE surface sediments, the determined gradients of pore water Ba isotopes, together with concentration variations of Ba and other redox-sensitive elements such as manganese (Mn), show that non-detrital excess Ba carriers including Mn oxides and authigenic barite clearly affect the post-depositional Ba dynamics. Stable Ba isotopes are thus a potentially powerful tracer of Ba geochemistry during early sediment diagenesis in estuarine depositional environments.

Plain Language Summary Dissolved barium (Ba) concentrations change with depth in sediment pore waters because of various chemical reactions involving the formation and dissolving of manganese (Mn) and barite ($BaSO_4$) minerals. The development of stable Ba isotope measurements provides a novel tool to better understand these reactions in sediment pore waters. Here, we measured the dissolved stable Ba isotopic compositions in sediment pore waters near the bottom of the Pearl River Estuary, China. Pore water Ba isotopic signatures generally decrease from the sediment surface downward. The change of Ba concentrations and isotopic compositions measured in the field is well reproduced by a chemical model including diffusion and mineral formation/dissolving processes. This change in pore water Ba isotopes results from a combination of different processes including Ba sticking to sediment particles formed during the cycling of Mn minerals and the formation of $BaSO_4$ minerals, which preferentially remove lighter Ba isotopes from the pore water into the solids. This is significant because it allows pore water Ba isotopes to be used to trace chemical reactions during Ba cycling in freshwater and marine sediments.

1. Introduction

Estuaries form the transition from freshwater to coastal marine environments and act as efficient reactors for many riverine trace elements before they reach the open ocean. While the formation of authigenic mineral phases in anoxic estuarine sediments enhances the removal of some trace elements, early diagenetic reactions can also release trace elements back into the water column via reductive processes (e.g., of manganese (Mn) and iron (Fe) oxides) or dissolution of barium (Ba) bearing solid phases (cf., Charette et al., 2005; Gingele et al., 1999; Haese et al., 2006; Henkel et al., 2012, 2016, 2018; Hong et al., 2018; McManus et al., 1998; Riedinger et al., 2006; Torres et al., 1996). Therefore, the functioning and efficiency of the estuarine reactor are strongly influenced by

early sediment diagenesis, which controls the dynamics of trace elements in the pore waters and their potential benthic fluxes into the overlying water column.

The estuarine behavior of Ba in the water column is characterized by a gradual increase in dissolved Ba concentrations from zero salinity to a maximum at low salinities around 5–10, generally ascribed to the salinity-induced desorption of Ba from fluvial suspended particles, which is followed by a linear decrease in concentrations with salinity further increasing toward the coastal marine environments (Edmond et al., 1985; Joung & Shiller, 2014). However, the apparently conservative Ba-salinity relationship beyond low salinities of 5–10 is potentially perturbed by benthic Ba inputs via the sediment-water interface in estuaries (Colbert & McManus, 2005; Hong et al., 2018; Joung & Shiller, 2014; McManus et al., 1998; Moore & Shaw, 2008; Scholz et al., 2023). Although previous studies have shown that the sedimentary Ba distributions are affected by various processes including transport of terrigenous detritus (i.e., the upper continental crust), adsorption-desorption associated with non-detrital particulate phases, and barite dissolution and precipitation (e.g., Charette et al., 2005; Gingele et al., 1999; Henkel et al., 2012; Riedinger et al., 2006; Torres et al., 1996), a better understanding of early diagenetic controls on Ba dynamics in sediment pore waters is still required.

Inspired by the pioneering study of von Allmen et al. (2010), stable Ba isotopes have been developed as a new tracer to investigate the (bio)geochemical cycling of Ba in marine environments. The majority of studies carried out so far have revealed measurable variations of dissolved Ba isotopic compositions in vertical seawater profiles and along the salinity gradient in estuaries (Bates et al., 2017; Bridgestock et al., 2018, 2021; Cao, Li, et al., 2020; Cao, Siebert, et al., 2020; Cao et al., 2016, 2021; Geyman et al., 2019; Hemsing et al., 2018; Horner et al., 2015; Hsieh & Henderson, 2017; Yu et al., 2022). Stable Ba isotopic signatures of the marine (as well as estuarine and fluvial) sedimentary solid phase are systematically lighter than seawater and vary within a relatively narrow range (Bridgestock et al., 2018, 2019; Charbonnier et al., 2020; Crockford et al., 2019; Nan et al., 2018; Nielsen et al., 2018; Scholz et al., 2023). In this context, the stable Ba isotope geochemistry of pore waters has rarely been examined but holds potential to elucidate sedimentary Ba dynamics during early diagenesis.

The Pearl River Estuary (PRE) is a large subtropical estuary significantly affected by human activities. A pronounced increase in anthropogenic loads of organic carbon and nutrients over the last few decades has led to the recent deterioration of aquatic environments, including the occurrence of water column hypoxia. Although extensive studies on hypoxia and their controlling mechanisms in the PRE are available (Dai et al., 2006; He et al., 2014; Li et al., 2020; Qian et al., 2018; Rabouille et al., 2008; Su et al., 2017; Zhao et al., 2021), information on sediment redox zonation and associated element cycling in the sediment pore waters is very sparse (Cai et al., 2015; Hong et al., 2018; L. Zhang, et al., 2013). With the goal to unravel the geochemical behavior of Ba isotopes in sediment pore waters and its potential controlling processes, we analyzed the depth distribution of stable Ba isotopic compositions in the pore waters ($\delta^{138}Ba_{pw}$) of PRE surface sediments together with other supporting geochemical parameters. The obtained Ba isotope distributions were then simulated using a diffusion-reaction model in order to evaluate pore water Ba isotope fractionation and identify its major controls in these deposits. By comparison of the $\delta^{138}Ba_{pw}$ signatures in the sediment surface with those in the overlying bottom waters of the PRE, we also assess whether benthic fluxes of Ba significantly affect the stable Ba isotopic composition in the water column of the estuarine mixing zone.

2. Materials and Methods

2.1. Study Area

The Pearl River (or Zhujiang) drains an area of 452,000 km^2 into the South China Sea with a water discharge of $\sim 3.3 \times 10^{11}$ m^3 y^{-1} (He et al., 2014; Qian et al., 2018). The PRE is generally divided into three zones (Figure 1): (a) the upper estuary: the channel flowing from the city of Guangzhou to the Humen outlet; (b) the middle estuary: the inner Lingdingyang from the Humen outlet to the inner Lingding Island; and (c) the lower estuary: the outer Lingdingyang from the inner Lingding Island to the outer estuary. In the upper reach of the PRE, pronounced year-round hypoxia occurs in the water column, primarily due to oxygen consumption by excessive discharge of organic matter and ammonia (Dai et al., 2006; He et al., 2014; Rabouille et al., 2008). In the lower reach of the PRE, sustained summer hypoxia develops in the bottom waters off Hong Kong, likely associated with elevated phytoplankton production stimulated by excessive nutrient inputs (Li et al., 2020; Qian et al., 2018; Su et al., 2017; Zhao et al., 2021).
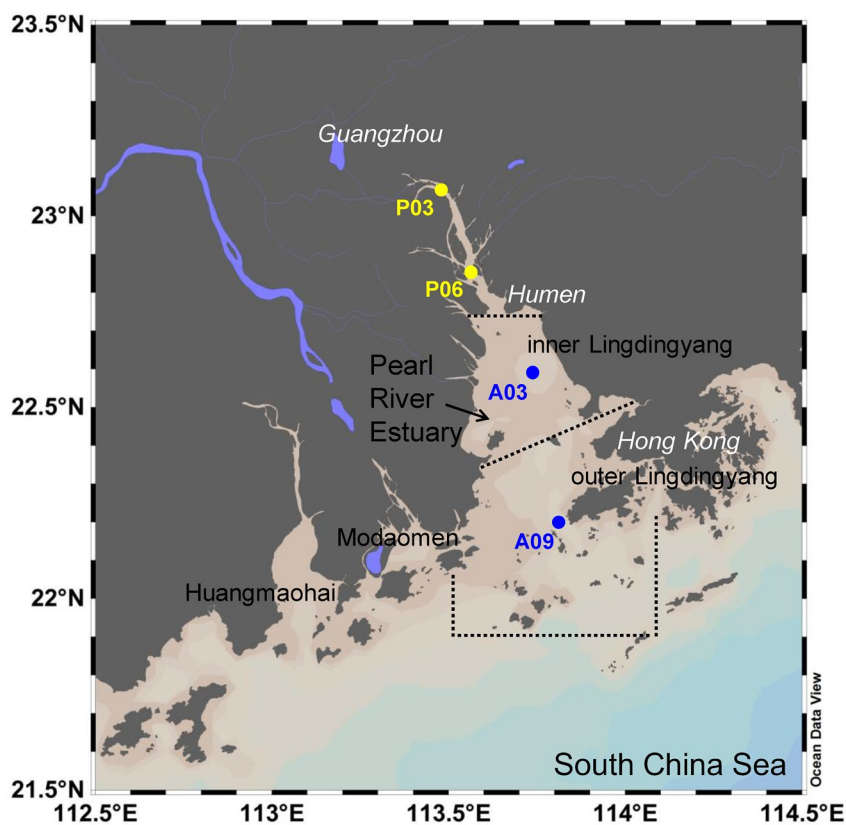
Figure 1. Map of the Pearl River Estuary showing the locations of sampling stations in January 2017. The estuary is divided into three zones: (1) the upper estuary (Humen upstream); (2) the middle estuary (inner Lingdingyang); and (3) the lower estuary (outer Lingdingyang and beyond).

The Pearl River delivers $\sim 8 \times 10^7$ tons of sediments annually, the majority of which is trapped within the estuary leading to high sedimentation rates of $>1–7$ cm y^{-1}. While the seabed of the PRE is dominated by fine-grained sediments, their grain size varies as a function of the hydrodynamics of the sedimentation environment. The bottom sediments are relatively coarse in the upper reaches, whereas the middle and lower estuarine sediments are composed of a mixture of silts and clays (Cai et al., 2015; He et al., 2010; W. Zhang et al., 2013). Pore water profiles of nutrients, dissolved inorganic carbon, and trace elements including Ba for sediments of the PRE have recently been reported by L. Zhang et al. (2013), Cai et al. (2015), and Hong et al. (2018), which mainly quantify the benthic flux of elements into the overlying water column. However, these studies do not include an in-depth discussion of the diagenetic element cycling as a function of sediment geochemical zonation.

2.2. Sampling and Analyses

2.2.1. Sampling

Surface sediment samples were collected at shallow water depth stations P03, P06, A03, and A09 (bottom depth of 5.8, 21.3, 10.5, and 15.3 m, respectively) located in the upper, middle, and lower estuary of the Pearl River during a winter cruise in January 2017 (Figure 1). Undisturbed sediment cores were obtained with a standard box corer ($30 \times 30 \times 60$ cm^3) and subsamples were collected by inserting PVC tubes (diameter 47 mm) into the box core. Sediment subcores were sliced into 1-cm thick slabs for analyses of metal concentrations, including Ba, Mn, Fe, and aluminum (Al) and total organic carbon (TOC) concentrations. Pore water samples were extracted from the sediment subcores using rhizon samplers (Seeberg-Elverfeldt et al., 2005). Aliquots for analyses of Ba concentrations and stable isotopic compositions, as well as of Mn, Fe, and sulfate (SO$_4^{2-}$) concentrations, were acidified with distilled concentrated HCl (0.2% v/v) and stored at room temperature. Aliquots for nitrate (NO$_3^-$) analyses were stored at $-20°C$. In addition, bottom water samples (2–3 m above the seafloor) at each station were

collected with Niskin bottles attached to a rosette sampler and were subsequently filtered and acidified for analyses of Ba concentrations and stable isotopic compositions, which were previously published by Cao et al. (2021).

2.2.2. Elemental Analyses of Pore Waters and Bottom Waters

Barium concentrations in the pore waters and bottom waters were analyzed using an isotope dilution method on an Agilent 7,700x quadrupole-ICP-MS with a precision of $\pm 1\%$ (1 standard deviation (1SD)). After diluting the samples 10–100 fold, pore water Mn and Fe concentrations were determined using an Agilent 7700x quadrupole-ICP-MS with a precision better than $\pm 5\%$ (1SD) and SO_4^{2-} concentrations were determined using a DIONEX ICS-1100 ion chromatograph with a precision of $\pm 1\%$ (1SD) based on external calibration standards. Concentrations of NO_3^- in the pore waters and bottom waters were determined using a Technicon AA3 Auto-Analyzer (Bran + Luebbe GmbH) following classical colorimetric methods with a detection limit of $0.1\,\mu mol\,L^{-1}$. The salinity of pore water samples was determined using a Multi 340i multi-parameter meter (WTW) and the salinity of bottom water samples was determined shipboard with a SBE25 Conductivity-Temperature-Depth (CTD) recorder (Sea-Bird).

2.2.3. Elemental Analyses of the Solid Phase

Approximately 10 mg of dried and powdered sediments were completely digested in a concentrated acid mixture of 0.45 mL HCl, 0.15 mL HNO_3, and 0.25 mL HF at 120°C for 24 hr. After evaporation to dryness and redissolution, the bulk Ba, Mn, Fe, and Al concentrations were determined using an Agilent 5110 ICP-OES with a precision better than $\pm 2\%$ (1SD) based on external calibration standards. After carbonate removal by reaction with 0.5 N HCl, TOC contents in the sediments were determined using a PE-2400 SERIES II CHNS/O analyzer with a precision better than $\pm 5\%$ (1SD). In addition, approximately 250 mg of selected sediment samples were sequentially extracted for Ba isotope determination of specific Ba carriers, including barite using 25 mL of a 2 N NH_4Cl and Mn and Fe oxides using 25 mL of a CDB solution (0.15 N Na-citrate, 0.5 N $NaHCO_3$ (pH 7.6), and 1.125 g Na-dithionite) (Plewa et al., 2006; Schenau et al., 2001).

2.2.4. Stable Barium Isotope Analyses

The stable Ba isotopic composition was measured using a double spike technique and is given in ‰ deviations relative to the international Ba standard NIST SRM 3104a $(Ba(NO_3)_2$, Lot: 070222; $\delta^{138}Ba = [(^{138}Ba/^{134}Ba)_{sample}/(^{138}Ba/^{134}Ba)_{standard}-1] \times 1000)$. The actual ^{138}Ba signal was not measured on a Nu Instruments HR MC-ICP-MS at Xiamen University because of its very high natural abundance of 71.70% relative to the other Ba masses, which would have caused the differences between the monitored voltages of different masses to be impractically large. We thus only report $\delta^{138}Ba$ values in this contribution (Figures 4–6) obtained by multiplying $\delta^{137}Ba$ by 1.33 assuming mass-dependent fractionation (Horner et al., 2015). A ^{130}Ba–^{135}Ba double spike was prepared from $^{130}BaCO_3$ and $^{135}BaCO_3$ (ORNL enriched to 35.8% and 93.4%, respectively) and was added to all water samples, as well as digested solutions of selected sediment samples by sequential extraction. After equilibration overnight, Ba was purified from the sample matrix using cation-exchange chromatography with an average yield of 90% for the entire chemical preparation procedure. The purified sample solutions were introduced as a dry aerosol into the plasma using a DSN-100 desolvator (Nu Instruments) and Ba isotopes were determined in static mode. A three-dimensional data reduction procedure was used and each spiked sample measurement of $\delta^{138}Ba$ was normalized to two "bracketing" spiked standard measurements (Cao, Li, et al., 2020).

Each pore water and sediment sample solution was analyzed three times (except one sample that was only analyzed twice and three samples that were analyzed six times) in a single measurement session resulting in sample reproducibility between ± 0.01 and $\pm 0.15‰$ for $\delta^{138}Ba$ (2SD; Tables S1 and S2 in Supporting Information S1), which represent the uncertainty of field data of this contribution (Figures 4–6). Repeated measurements of four in-house standards between April 2017 and January 2023 gave average $\delta^{138}Ba$ values of $-0.05 \pm 0.04‰$ (2SD, $N = 19$; $Ba(NO_3)_2$ standard solution, Inorganic Ventures), $+0.10 \pm 0.05‰$ (2SD, $N = 29$; IAEA-SO-5, $BaSO_4$, IAEA), $+0.08 \pm 0.05‰$ (2SD, $N = 26$; IAEA-SO-6, $BaSO_4$, IAEA), and $+0.38 \pm 0.05‰$ (2SD, $N = 15$; seawater collected at 500 m depth in the South China Sea basin). The long-term external 2SD reproducibility was $\pm 0.05‰$.

Our measurements of two artificially fractionated Ba isotope standards yielded $\delta^{138}Ba$ of $-1.53 \pm 0.06‰$ (2SD, $N = 4$) for BaBe12 and of $-0.83 \pm 0.07‰$ (2SD, $N = 7$) for BaBe27, both of which are within analytical error indistinguishable from the values (BaBe12: $-1.54 \pm 0.07‰$ and BaBe27: $-0.82 \pm 0.07‰$) reported by van Zuilen,

Nägler, and Bullen (2016). We also analyzed the GEOTRACES SAFe seawater reference material. Our δ^{138}Ba data (surface: $+0.62 \pm 0.04$‰, 2SD, $N = 2$ and deep: $+0.28 \pm 0.09$‰, 2SD, $N = 2$) are identical to those obtained from three other labs (surface: $+0.62 \pm 0.02$‰ and deep: $+0.27 \pm 0.02$‰ (Hsieh & Henderson, 2017); surface: $+0.63 \pm 0.04$‰ and deep: $+0.32 \pm 0.03$‰ (Geyman et al., 2019); deep: $+0.27 \pm 0.03$‰ (Yu et al., 2020)).

2.3. Barite Saturation State Calculation

The barite saturation state (BSS) of pore waters was calculated as follows:

$$\text{BSS} = \frac{(\text{IP})_{\text{in-situ}}}{(K_{\text{sp}})_{\text{in-situ}}} \tag{1}$$

$(\text{IP})_{\text{in-situ}}$ denotes the in situ ionic product estimated based on the dissolved Ba and SO_4^{2-} concentrations in the pore waters. $(K_{\text{sp}})_{\text{in-situ}}$ denotes the in situ stoichiometric solubility product of barite as a function of temperature, salinity, and pressure deduced by Monnin (1999) and Rushdi et al. (2000). BSS > 1 indicates oversaturation favoring barite precipitation, while BSS < 1 indicates undersaturation promoting barite dissolution.

2.4. Estimation of Stable Barium Isotope Fractionation

A diffusion-reaction model was used to estimate the stable Ba isotope fractionation factor ($^{138}\varepsilon$) in the pore waters of the PRE. Given that estuaries are highly dynamic environments with various physical and biogeochemical processes exerting complex influences, we started using a simplified model assuming that the observed pore water profiles in winter are yearly averaged in steady state conditions and neglected the effect of pore water advection due to burial, compaction, bioturbation, and bioirrigation. The one-dimensional equation used is given by the following equation:

$$\frac{\partial}{\partial z}\left(\varphi D_S \frac{\partial C}{\partial z}\right) + R = 0 \tag{2}$$

where C is the pore water concentration, z is the depth, φ is the porosity, D_S is the effective diffusivity in the sediment, and R is the net transformation rate between pore water and solid phase. The molecular diffusion coefficient (D_0), calculated by the temperature and salinity dependent relations (Boudreau, 1997), was corrected by a factor that reflects the effect of the tortuosity to obtain D_S (Iversen & Jørgensen, 1993):

$$D_S = \frac{D_0}{1 + 3 \times (1 - \varphi)} \tag{3}$$

The transformation rate R was calculated from measured pore water Ba profiles using a complementary steady state model, PROFILE (Berg et al., 1998). The porosity φ was applied using an average value in each core. Concentrations at the top and bottom of the calculation domain were fixed to field-measured values. The PROFILE model found a series of fit curves to the Ba concentration profiles subdivided in a number of zones and provided R values for each zone. $R > 0$ indicates net Ba release from the solid phase into the pore waters, while $R < 0$ indicates net Ba removal from the pore water into the solid phase. $R = 0$ suggests that pore water Ba distributions are mainly controlled by diffusion within certain zones with negligible influence of solution-solid phase interactions.

We calculated absolute concentrations for pore water ^{138}Ba and ^{134}Ba, which were separately computed using the diffusion-reaction equation (Equation 2). Since the transformation rate R obtained by the PROFILE model was based on total Ba (all isotopes), the rate contributed from ^{138}Ba and ^{134}Ba (R_{Ba}^{138} and R_{Ba}^{134}, respectively) was calculated according to Equations 8–11, which is discussed in detail below. The sum of ^{138}Ba and ^{134}Ba concentrations was finally converted to the total Ba concentration. To consider potential isotope fractionation during Ba diffusion in sediments (van Zuilen, Müller, et al., 2016), a dimensionless exponent β was applied:

$$\frac{D_{134}}{D_{138}} = \left(\frac{138}{134}\right)^{\beta} \tag{4}$$

Removal of Ba from the pore water to the solid phase via precipitation or adsorption is assumed to follow first order kinetics with isotope fractionation (Böttcher et al., 2012, 2018; von Allmen et al., 2010):

$$R_{\text{Ba}}^{134} = {}^{134}k\,{}^{134}Ba \tag{5}$$

$$R_{Ba}^{138} = {}^{138}k\,{}^{138}Ba \tag{6}$$

$$\frac{R_{Ba}^{134}}{R_{Ba}^{138}} = \alpha \frac{{}^{134}Ba}{{}^{138}Ba} \tag{7}$$

where ${}^{134}k$ and ${}^{138}k$ are the rate constants of each species and the fractionation factor α is defined as their ratio. α can be converted to the epsilon notation ${}^{138}\varepsilon$ (in ‰) by $(1/\alpha - 1) \times 1000$. Rearranging above equations gives the specific rates of each isotope:

$$R_{Ba}^{134} = \frac{\alpha^{134}Ba}{{}^{138}Ba + \alpha^{134}Ba} \times \left(R_{Ba}^{138} + R_{Ba}^{134}\right) \tag{8}$$

$$R_{Ba}^{138} = \frac{{}^{138}Ba}{{}^{138}Ba + \alpha^{134}Ba} \times \left(R_{Ba}^{138} + R_{Ba}^{134}\right) \tag{9}$$

von Allmen et al. (2010) found that partial dissolution of $BaSO_4$ does not significantly affect the Ba isotopic composition of a fluid if at least 10% of the solid dissolves. Mavromatis et al. (2016) suggested that no Ba isotope fractionation occurs during $BaCO_3$ dissolution but stated that their data cannot adequately rule out fractionation at the onset of dissolution. Bridgestock et al. (2019) based their assumption of absent Ba isotope fractionation during barite dissolution on the relatively constant particulate Ba isotopic signatures in the upper 1,000 m of the South Atlantic (Horner et al., 2017). Despite debates, we assumed in this simplified model that release of Ba from the solid phase to the pore water via dissolution or desorption is not accompanied by significant Ba isotope fractionation. The transformation rates used are as follows:

$$R_{Ba}^{134} = \frac{1}{1 + r_{sp}} \times \left(R_{Ba}^{138} + R_{Ba}^{134}\right) \tag{10}$$

$$R_{Ba}^{138} = \frac{r_{sp}}{1 + r_{sp}} \times \left(R_{Ba}^{138} + R_{Ba}^{134}\right) \tag{11}$$

where r_{sp} is the ratio of ${}^{138}Ba$ to ${}^{134}Ba$ in the solid phase and can be converted to a Ba isotopic composition of particulate Ba phases ($\delta^{138}Ba_{sp}$) mainly interacting with the pore waters. Our measurements of sediment $\delta^{138}Ba$ signatures via sequential extraction ($\delta^{138}Ba_{sed}$) ranged between 0.00 and +0.12‰ (Table S2 in Supporting Information S1).

Because $^{138}\varepsilon$, β, and $\delta^{138}Ba_{sp}$ are largely unknown for sediments in natural environments to date, different values of these parameters were tested and assigned in the model to derive optimized ones. The criterion is that the fitting process finds a minimum error compared to the field measurements (i.e., error $\approx \sum(\delta^{138}Ba_{observation} - \delta^{138}Ba_{model})^2$). Our diffusion-reaction model was thus run over a wide range of $^{138}\varepsilon$ (−0.40, −0.50, −0.60, and −0.70‰), β (−0.005, 0.000, 0.005, and 0.010), and $\delta^{138}Ba_{sp}$ (0.00, +0.03, +0.05, +0.10, and +0.12‰), and the best fit values were obtained by reaching the minimum error.

3. Results

3.1. Pore Water Element Profiles

At the upstream PRE station P03, pore water NO_3^- concentrations decrease from 5.6 μmol L^{-1} in the sediment surface to near zero below 10 cm core depth (Figure 2a). Pore water Mn concentrations steadily increase with depth until the base of the core (from 10 to 88 μmol L^{-1}), while Fe concentrations increase to 10 cm depth and remain stable below at ~320 μmol L^{-1}. The SO_4^{2-} profile shows a convex-downward shape with concentrations decreasing from 0.7 mmol kg^{-1} within the topmost sample to values around zero below 8 cm depth (Table S3 in Supporting Information S1). The Ba profile shows an increasing trend with depth, with Ba concentrations steeply increasing below 8 cm core depth reaching >1,000 nmol kg^{-1} (Figure 2a).

At the upper PRE station P06, the complete consumption of NO_3^- at 3 cm (from 62.2 to 1.8 μmol L^{-1}) is followed by the reduction of Mn and Fe oxides as evidenced by the release of dissolved Fe and Mn into the pore waters. Pore water Mn and Fe concentrations both peak at 4–5 cm core depth displaying concentrations of ~165 and ~490 μmol L^{-1}, respectively (Figure 2b). While Mn concentrations slightly decrease again below
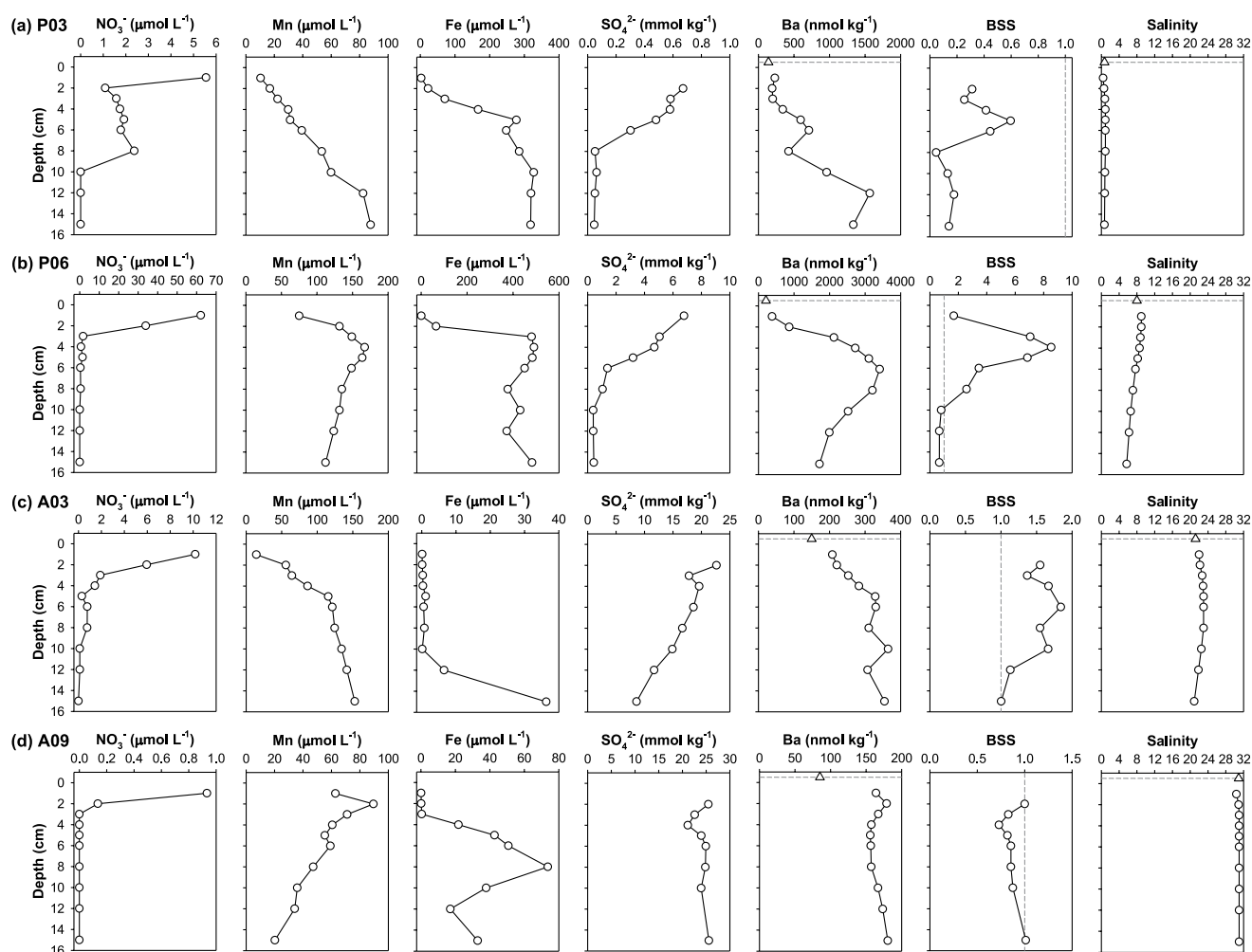
Figure 2. Pore water profiles of dissolved NO_3^-, Mn, Fe, SO_4^{2-}, and Ba concentrations, barite saturation state (BSS), and salinity. (a) station P03; (b) station P06; (c) station A03; (d) station A09. Triangles indicate data collected in the bottom waters 2–3 m above the seafloor. The gray vertical dashed line denotes BSS = 1. Note that the concentration ranges for the different parameters, except for salinity, differ strongly among stations.

reaching ~120 μmol L^{-1}, Fe concentrations remain essentially stable and only fluctuate between high values of 380 and 480 μmol L^{-1}. The shape of the pore water SO_4^{2-} profile is similar to that at station P03. However, SO_4^{2-} concentrations of 6.8 mmol kg^{-1} in the sediment surface are a factor of 10 higher than at station P03 due to the higher salinity of the pore water (Figure 2b). Sulfate concentrations steeply decrease downward within the upper 6 cm and display a less steep downward decline below, reaching SO_4^{2-} concentrations of 0.4 mmol kg^{-1} at the base of the core (Table S3 in Supporting Information S1). Dissolved Ba exhibits a maximum concentration of 3,410 nmol kg^{-1} at 6 cm depth and decreases both below (reaching 1,720 nmol kg^{-1} at the base of the core) and above (reaching 210 nmol kg^{-1} in the sediment surface) this depth (Figure 2b).

At the middle PRE station A03, pore water NO_3^- concentrations decrease strongly in the upper 5 cm (from 10.2 to 0.3 μmol L^{-1}) followed by a less steep decline down until 10 cm depth, which is mirrored by the pore water profile of Mn increasing from 14 to 153 μmol L^{-1} with depth (Figure 2c). Pore water Fe concentrations are close to detection limit within the upper 10 cm and sharply increase below 10 cm until the base of the core reaching 36 μmol L^{-1} indicating the reduction of Fe oxides. Pore water SO_4^{2-} concentrations slightly decrease downward from values even higher than at the two upstream sites (22.7 mmol kg^{-1} at 2 cm depth to 8.6 mmol kg^{-1} at the base of the core; Table S3 in Supporting Information S1). Pore water Ba concentrations vary within a much narrower range than at the two upstream sites and generally increase with depth until 5–6 cm (from 150 to 330 nmol kg^{-1}), below which Ba distributions fluctuate between 40 and 50 nmol kg^{-1} (Figure 2c).

At the lower PRE station A09, pore water NO_3^- is also completely consumed at 3 cm and Mn exhibits a maximum concentration of 90 µmol L^{-1} at 2 cm. Iron concentrations are close to detection limit within the uppermost 3 cm (Figure 2d). Below this zone, Mn concentrations decrease with depth, while Fe concentrations display a maximum of 74 µmol L^{-1} at 8 cm depth indicating Fe reduction. Sulfate concentrations are nearly constant at 25.0 mmol kg^{-1} over the entire depth of the profile (Table S3 in Supporting Information S1). Barium shows a small concentration maximum of 172 nmol kg^{-1} at 2–3 cm coincident with the Mn peak, below which Ba concentrations slightly decrease until 5–6 cm. In contrast to the continuous downward decline of Mn, pore water Ba shows a slight increasing trend below 6 cm reaching 180 nmol kg^{-1} at the base of the core (Figure 2d).

3.2. Solid Phase Element Profiles

The bulk Ba, Mn, Fe, and Al contents in the sedimentary solid phase (Table S4 in Supporting Information S1), overall comparable among the four investigated PRE stations, are similar to the element composition of the upper continental crust (i.e., Ba ~ 0.6, Mn ~ 0.7, Fe ~ 37, and Al ~ 81 mg g^{-1}; Rudnick & Gao, 2014). The bulk TOC contents in the sedimentary solid phase (Table S4 in Supporting Information S1) vary within a range of 0.3%–1.4% and are overall higher at the upstream station P03 than at the other three stations (Figure 3). While the depth distribution of Ba, Mn, and Fe largely follows that of Al in the solid phase, the majority of the element to Al ratios are lower than or comparable to the average value for the upper continental crust (Rudnick & Gao, 2014; Taylor & McLennan, 1985). These features point to the dominant detrital background of the PRE surface sediments. Exceptions are the Fe/Al ratio in the solid phase at stations P06 and A09, where non-detrital excess Fe contributes to a relatively large portion of total Fe in the two cores (Figures 3b and 3d).

Reitz et al. (2004) reported an average detrital Ba/Al ratio of 0.0037 for pelagic surface sediments, which is a factor of 2 lower than that of the upper continental crust (0.0068 or 0.0077; Rudnick & Gao, 2014; Taylor & McLennan, 1985). The Ba/Al ratios throughout cores A03 and A09 are close to the value of 0.0037 with very little variations (with the exception of one peak in the upper centimeters of core A09; Figures 3c and 3d). In contrast, cores P03 and P06 show systematic variations in Ba/Al ratios and larger parts of the cores have elevated values with respect to the pelagic endmember (Figures 3a and 3b). Similarly, variations of solid phase Mn/Al and Fe/Al ratios, as well as TOC concentrations, are significantly larger at stations P03 and P06 than at stations A03 and A09 (Figure 3).

3.3. Stable Barium Isotope Distributions in the Pore Waters

Bottom water salinity generally increases from near zero at the upstream station P03 to 30.9 at the lower station A09. At each station, pore water salinity is almost constant over depth and close to the respective bottom water salinities. In contrast, pore water Ba concentrations are significantly higher than those of the corresponding overlying bottom waters (Figure 2). Except for station A09, the pore water $\delta^{138}Ba_{pw}$ signature in the topmost sediment layer is significantly heavier than in the bottom waters, while $\delta^{138}Ba_{pw}$ profiles at all four stations generally show a decline with depth and overall mirror Ba concentration patterns (Figure 4).

Taking a closer look at each single profile, a lightest $\delta^{138}Ba_{pw}$ signature of +0.13‰ corresponds to a maximum Ba concentration at 12 cm depth at station P03. Above 12 cm core depth, $\delta^{138}Ba_{pw}$ values gradually increase to +0.47‰ in the sediment surface, mirrored by generally decreasing Ba concentrations (Figures 2a and 4a). At station P06, the lightest $\delta^{138}Ba_{pw}$ signatures averaging +0.13 ± 0.03‰ are observed at 5–8 cm core depth (1SD, $N = 3$; Table S1 in Supporting Information S1), which coincide with the pronounced Ba concentration maximum at 6 cm. Above this maximum pore water $\delta^{138}Ba_{pw}$ values sharply increase to +0.51‰ in the sediment surface, whereas below 6 cm the Ba isotopic signature values slowly increase to +0.22‰ at the base of this core (Figures 2b and 4b).

The $\delta^{138}Ba_{pw}$ at station A03, showing a distribution pattern inverse to that of Ba concentrations, decreases rapidly from +0.69 to +0.28‰ between 2 and 6 cm and reaches a second minimum of +0.27‰ at the base coinciding with elevated Ba concentrations (Figures 2c and 4c). At station A09, the lightest $\delta^{138}Ba_{pw}$ of +0.24‰ is also observed at the base of the core and corresponds to the highest pore water Ba concentration, whereas the Ba concentration maximum at 2 cm is not reflected by a $\delta^{138}Ba_{pw}$ minimum. Both Ba concentrations and $\delta^{138}Ba_{pw}$ vary only within a narrow range over the entire depth of this core (150–174 nmol kg^{-1} and +0.24-+0.49‰, respectively) relative to the other three cores (Figures 2d and 4d).
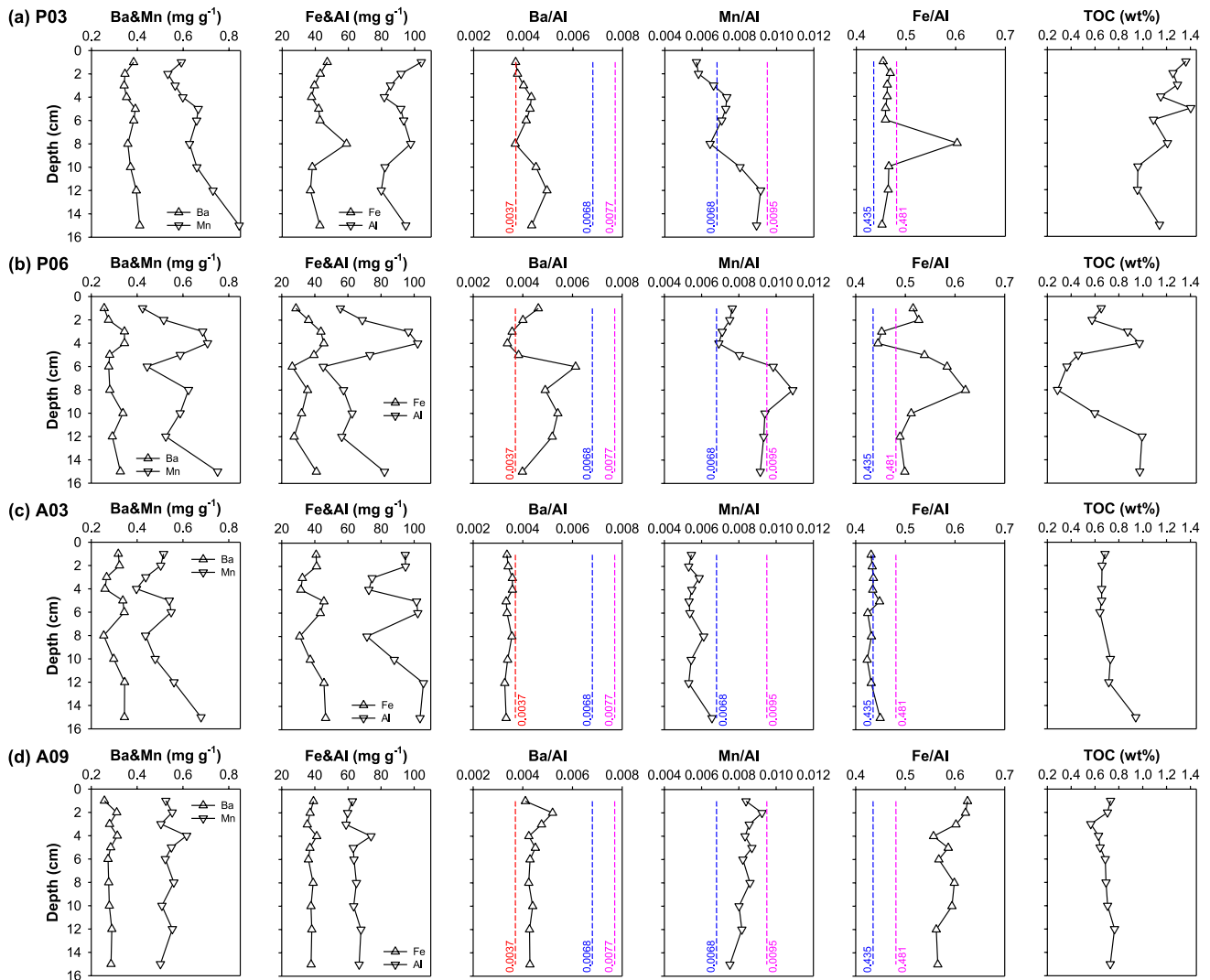
Figure 3. Solid phase profiles of bulk Ba, Mn, Fe, and Al concentrations, Ba/Al, Mn/Al, and Fe/Al ratios, and total organic carbon (TOC) concentrations. (a) station P03; (b) station P06; (c) station A03; (d) station A09. The red dashed line and the number denote the average detrital Ba/Al ratio for pelagic surface sediments (Reitz et al., 2004). The blue dashed line and the number denote the average X/Al ratio (X is Ba, Mn, or Fe) for the upper continental crust reported by Taylor and McLennan (1985), while the pink dashed line and the number denote the composition of the upper continental crust updated by Rudnick and Gao (2014).

4. Discussion

4.1. Processes Controlling Barium Dynamics in the Sediment Pore Waters of the Pearl River Estuary

Although terrigenous detritus dominates the PRE surface sediments, the measurable concentration and isotope gradients in pore water Ba profiles indicate that non-detrital particulate Ba phases, though very minor in comparison to the detrital phase, clearly affect Ba dynamics at all sites. Moreover, the differences in the pore water and solid phase element profiles between the study sites evidently suggest the control of a variety of geochemical processes associated with different sediment redox zonation and depths of reaction fronts. With the combination of the net transformation rate (R) obtained by the diffusion-reaction model, we discuss potential solution-solid phase interactions in the sediments at each site.

At the upstream PRE station P03, overall high pore water Mn and Fe concentrations, which fall into a range similar to those observed in other coastal surface sediments (e.g., Henkel et al., 2016, 2018; Oni et al., 2015; Schnakenberg et al., 2021; Vosteen et al., 2022; Wunder et al., 2021), suggest a suboxic zone characterized by the reduction of NO_3^-, Mn, and Fe (e.g., Kasten et al., 2003) in the uppermost 8–10 cm (Figure 2a). The
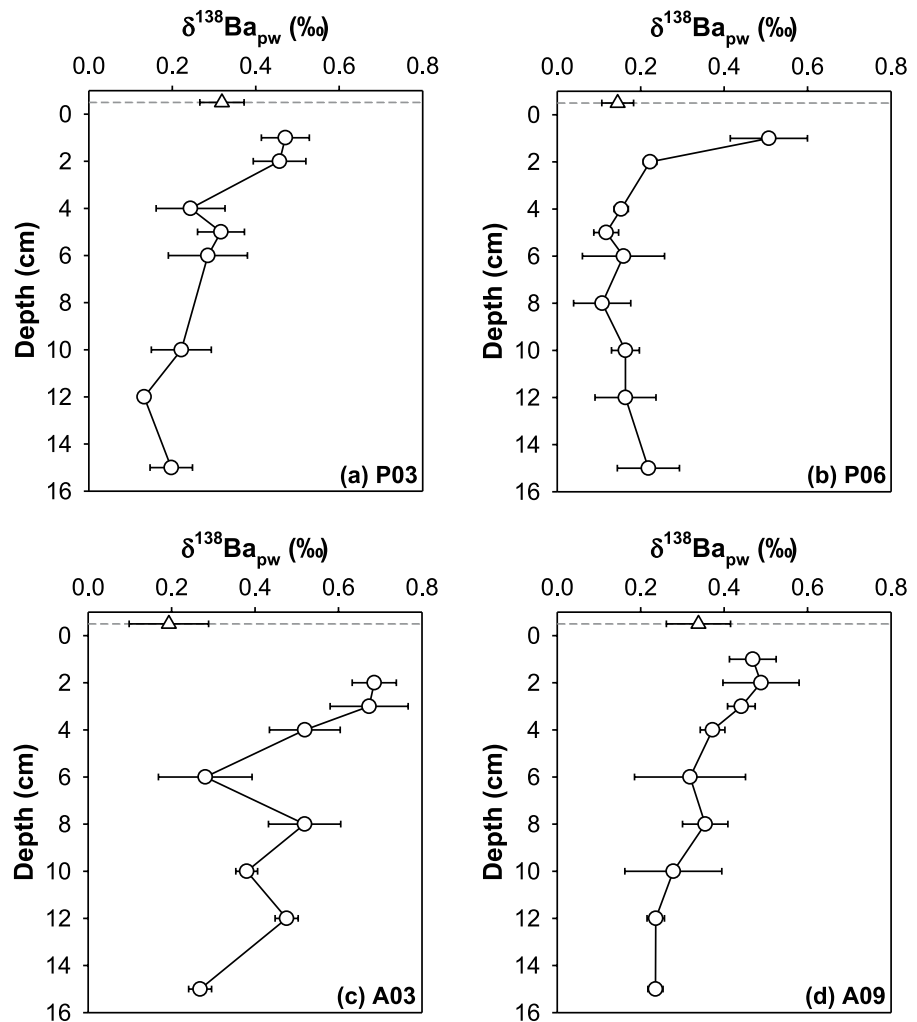
Figure 4. Pore water profiles of stable barium isotopic compositions ($\delta^{138}Ba_{pw}$). (a) station P03; (b) station P06; (c) station A03; (d) station A09. Triangles indicate data collected in the bottom waters 2–3 m above the seafloor.

diffusion-reaction model predicts a near zero R in the sulfate-depleted zone below 8 cm (Figure 5a), where pore water Ba concentration distributions are thus mainly controlled by the diffusion of Ba from highly concentrated pore waters of deeper sediments rather than in situ solution-solid phase interactions. Positive R values (+0.009 nmol cm^{-3} d^{-1}; Figure 5a) were obtained around 6 cm, suggesting net Ba release into the pore water. However, negative R values (−0.008 nmol cm^{-3} d^{-1}; Figure 5a) were obtained immediately above the uppermost 5 cm, suggesting that net Ba removal from the pore water and incorporation into the solid phase mainly occurs above this core depth. Such Ba release and removal processes are most likely driven by release via reductive dissolution of Mn oxides and subsequent adsorption onto authigenic Mn oxides (e.g., Charette et al., 2005; Gingele et al., 1999), as evidenced by the distribution pattern of the solid phase Ba/Al ratio similar to that of the Mn/Al ratio in this core (Figure 3a).

At the upper PRE station P06, a distinct pore water Mn peak and high Fe concentrations (Figure 2b) characterize the suboxic zone. Several peaks in solid phase Mn/Al and Fe/Al ratios above the detrital background (Figure 3b) indicate non-steady state accumulation of these metals, possibly related to temporal changes in dissolved Mn and Fe removal within the estuarine salinity gradient. The depth distribution of both pore water Ba and the solid phase Ba/Al ratio generally follows that of Mn over the entire depth of this core, suggesting that at this site Ba mobilization is also to a large extent related to diagenetic Mn cycling (e.g., Charette et al., 2005; Gingele et al., 1999). The dissolved Ba displaying maximum concentrations at 6 cm depth suggests that pore water Ba therein mainly results from reductive dissolution of Mn oxides, which corresponds to the model derived R values

Figure 5. Model results (lines) versus field measurements (symbols) of pore water Ba concentrations and isotopic compositions ($\delta^{138}Ba_{pw}$). (a) station P03; (b) station P06; (c) station A03; (d) station A09. A Ba isotope fractionation factor of −0.60‰ was employed for each core in the diffusion-reaction model. Gray solid lines denote the model-derived transformation rate R (Equation 2). Triangles indicate data collected in the bottom waters 2–3 m above the seafloor.

Figure 6. Sensitivity test of the diffusion-reaction model for estimating Ba isotope fractionation in the sediment pore waters at station P06. Lines denote model results of pore water Ba isotopic compositions ($\delta^{138}Ba_{pw}$) and symbols denote field measurements of $\delta^{138}Ba_{pw}$. (a) modeled $\delta^{138}Ba_{pw}$ for different Ba isotope fractionation factors ($^{138}\varepsilon$) when the Ba isotopic composition of non-detrital solid phase ($\delta^{138}Ba_{sp}$) is set to +0.03‰; (b) modeled $\delta^{138}Ba_{pw}$ for different $\delta^{138}Ba_{sp}$ when $^{138}\varepsilon$ is set to −0.60‰; (c) modeled $\delta^{138}Ba_{pw}$ without ($\beta = 0.000$) and with ($\beta = -0.005$, 0.005, and 0.010) a diffusion isotope effect when $^{138}\varepsilon$ is set to −0.60‰ and $\delta^{138}Ba_{sp}$ is set to +0.03‰.

of +0.09 nmol cm^{-3} d^{-1}. The transformation rate (R) values are around −0.07 nmol cm^{-3} d^{-1} in the upper 3 cm (Figure 5b), indicating net Ba removal. This is most likely induced by adsorption onto authigenic Mn (oxyhydr) oxides precipitating at the Mn redox boundary, that is, the oxic/suboxic boundary (e.g., Charette et al., 2005; Gingele et al., 1999). Another possible process is the precipitation of authigenic barite in the oversaturated pore waters above 6 cm depth, where the barite saturation state is markedly higher than 1 (Figure 2b). In contrast, R values are near zero below 6 cm of this core (Figure 5b) suggesting that Ba concentration distributions therein are mainly controlled by diffusion.

At the middle PRE station A03, the surface sediments consist almost entirely of detrital material, showing the lowest solid phase Ba/Al, Mn/Al, and Fe/Al ratios among the four sites (Figure 3c). Nevertheless, the distinct concentration gradients of Ba and other elements (Figure 2c) indicate that the non-detrital excess Ba carriers still play a role in this core to some extent. This is reflected by changing R values in the diffusion-reaction model (Figure 5c), which suggest release of Ba into the pore water at 5–6 cm core depth and subsequent removal above this core depth. The pore water barite saturation state is higher than 1 over the entire depth of the core (Figure 2c), suggesting the effects of barite precipitation (e.g., Gingele et al., 1999; Henkel et al., 2012; Riedinger et al., 2006; Torres et al., 1996).

At the lower PRE station A09, the distribution pattern of both the pore water Ba and the solid phase Ba/Al ratio above 4 cm depth mimics those of Mn (Figures 2d and 3d). The coupling between early diagenetic cycling of Ba and Mn at this site is thus apparently confined to the uppermost centimeters of the sediments (e.g., Charette et al., 2005; Gingele et al., 1999), where the model derived non-zero R values suggest effects of solution-solid phase interactions. The Ba distribution in the pore waters below 4 cm depth is mainly controlled by diffusion indicated by near zero R values (Figure 5d).

Due to the dominant detrital background of the PRE surface sediments, the solid phase Ba contents (0.3–0.4 mg g^{-1} or 2–3 mmol kg^{-1}) are comparable among the four sites (Figure 3). Pore water Ba concentrations are overall 3–4 orders of magnitude lower than those of the solid phase (Figures 2 and 3), implying that any changes in the former are too small to significantly impact the latter. However, the depth distribution of Ba concentrations overall resembles that of Mn concentrations in both the pore waters and the solid phase at all sites. These observations indicate that despite the dominance of detrital material, solution-solid phase interactions driven by early diagenetic processes, primarily redox cycling of Mn, occur in certain layers of the surface sediments, which are characterized by non-zero values of the transformation rate R (Figure 5).

4.2. Stable Barium Isotope Fractionation in the Sediment Pore Waters of the Pearl River Estuary

At the upstream PRE station P03, dissolved Ba diffuses upwards from the base of the core, showing a minimum $\delta^{138}Ba_{pw}$ signature of +0.13‰ and a maximum Ba concentration at 12 cm (Figures 2a and 4a). Barium is suggested to be mainly removed by adsorption onto authigenic Mn oxides (Charette et al., 2005; Gingele et al., 1999; Henkel et al., 2012) in the upper 5 cm, which preferentially transfers lower-mass Ba isotopes into the solid phase leading to the heaviest $\delta^{138}Ba_{pw}$ close to +0.5‰ in the sediment surface (Figure 4a). In the diffusion-reaction model, a best fit to field-measured $\delta^{138}Ba_{pw}$ data was obtained for a $^{138}\varepsilon$ of −0.60‰, a β of 0.000 (i.e., no isotope fractionation during diffusion), and a $\delta^{138}Ba_{sp}$ of +0.03‰ (Figure 5a; Equations 7–11).

At the upper PRE station P06, the highly Ba-enriched pore waters at 5–8 cm depth show the lightest $\delta^{138}Ba_{pw}$ signature, which is most likely driven by the release of low-mass Ba isotopes via reductive dissolution of metal oxides in the Mn-rich zone. The profile indicates both upward and downward diffusion, during which we suggest that significant amounts of Ba with lighter isotopic composition are adsorbed onto Mn oxides or removed by the precipitation of authigenic barite above the pore water Ba concentration maximum (Figures 2b and 4b). In the diffusion-reaction model, R varies within a range that is one order of magnitude higher than that at station P03, mainly resulting from the steeper pore water Ba concentration gradient at this site. However, a best fit to pore water Ba isotopic compositions was obtained for a $^{138}\varepsilon$ of −0.60‰, a β of 0.000, and a $\delta^{138}Ba_{sp}$ of +0.03‰ (Figure 5b; Equations 7–11), all of which are the same as those for station P03.

We thus used the three values to model the Ba isotope data of the sediment pore waters at the other two sites. At the middle PRE station A03, model results do not fit the field-measured values very well, probably due to the more scattered distribution of $\delta^{138}Ba_{pw}$ (Figure 5c). Moreover, the $\delta^{138}Ba_{pw}$ variation over the entire depth of this core is similar to that of station P06, whereas the Ba concentration range is notably smaller. This contrast implies a larger Ba isotope fractionation than indicated by the assigned $^{138}\varepsilon$. At the lower PRE station A09, however, the

diffusion-reaction model reproduces the field-measured data much better (Figure 5d). Values and ranges of R are the lowest as constrained by the smallest variation of pore water Ba concentrations. Correspondingly, $\delta^{138}Ba_{pw}$ also shows the smallest variation over the entire core, which is consistent with the predictions of the model. This consistency suggests that our selection of $^{138}\varepsilon$ (−0.60‰), β (0.000), and $\delta^{138}Ba_{sp}$ (+0.03‰) is reasonable.

A sensitivity test was conducted based on the data from station P06 because this site shows the largest pore water Ba concentration gradients accompanied by significant Ba isotope fractionation resulting from redox cycling of Mn and/or precipitation of authigenic barite. Model predictions generally match field $\delta^{138}Ba_{pw}$ of the pore waters despite a change of ±0.10‰ in the $^{138}\varepsilon$, while using a smaller $^{138}\varepsilon$ value of −0.40‰ the model merely fails to fit the heaviest $\delta^{138}Ba_{pw}$ signature in the sediment surface (Figure 6a). The isotope fractionation effect during Ba adsorption onto Mn (or Fe) oxides has not yet been independently constrained, whereas the $^{138}\varepsilon$ during barite and $BaCO_3$ or $BaMn(CO_3)_2$ formation has been reported to be −0.20 to −0.45‰ and −0.10 to −0.45‰, respectively, as deduced from laboratory experiments via precipitation and transformation (e.g., from aragonite to witherite and from gypsum to barite; Böttcher et al., 2012, 2018; von Allmen et al., 2010). Field measurements showed a fractionation that ranges between −0.30 and −0.60‰ during dissolved Ba removal in the water column of the ocean, estuaries, and a lake (Bates et al., 2017; Bridgestock et al., 2018, 2021; Cao, Li, et al., 2020; Cao, Siebert, et al., 2020; Cao et al., 2021; Horner et al., 2015, 2017; Hsieh & Henderson, 2017). Our model estimates of $^{138}\varepsilon$ (−0.60 ± 0.10‰) in the PRE pore water profiles, which need further validation by laboratory experiments or field measurements, are within error consistent with or slightly larger than these previously reported values. Note that any $^{138}\varepsilon$ observed in a natural environment is not a tightly constrained value but is the result of a combination of different processes fractionating Ba isotopes including particle adsorption, barite precipitation, and diffusion.

A change of ±0.08‰ in the $\delta^{138}Ba_{sp}$, slightly smaller than that in the $^{138}\varepsilon$, predicts relatively larger variations of $\delta^{138}Ba_{pw}$ signatures, which are, however, still within error consistent with field measurements (Figure 6b). Our measurements of extracted $\delta^{138}Ba_{sed}$ for several PRE sediment samples (P03-12 cm, P06-6 cm, A03-1 cm, and A09-2 cm; Table S2 in Supporting Information S1) indeed fall into the range of model derived $\delta^{138}Ba_{sp}$ (+0.03 ± 0.08‰), while those of +0.07 to +0.11‰ specifically for Ba associated with Mn and Fe oxides are slightly heavier than the best fit value of +0.03‰. Moreover, $\delta^{138}Ba_{sed}$ signatures of barites (0.00 to +0.12‰) obtained in this study generally agree with previous observations of both pelagic and terrigenous barites (averages of +0.04 ± 0.06‰ and +0.12 ± 0.31‰, respectively; Crockfort et al., 2019). However, the exact dominant non-detrital solid phases interacting with pore waters in each core, which are primarily inferred here from the concentration distribution of Ba and other redox-sensitive elements in both the pore waters and the solid phase, are still unclear. This prevents us from properly and independently estimating fractionation of Ba isotopes associated with a specific authigenic fraction using the diffusion-reaction model, which requires further dedicated examination of the Ba isotopic compositions of relevant solid phases.

Note that if the diffusion isotope effect (i.e., $\beta \neq 0.000$) is included, model results of $\delta^{138}Ba_{pw}$ indeed deviate from field measurements (Figure 6c). However, van Zuilen, Müller, et al. (2016) found that due to lower molecular weight, the diffusion coefficient of ^{134}Ba is larger than ^{138}Ba during dissolved Ba diffusion through a porous silica hydrogel, which generates a dimensionless exponent β of 0.010–0.011. This contrast may result from the difference in mineral structure between sediments in natural environments and silica hydrogel under laboratory conditions (Gong et al., 2019; Gou et al., 2020), or from the reduced effective mass difference of the strongly bounded multi-ion complexes between dissolved ^{138}Ba and ^{134}Ba in sediment pore waters (Bourg et al., 2010). Constraining β values for actual estuarine and pelagic sediments warrants future investigations.

4.3. Implications for Benthic Inputs of Stable Barium Isotopes in the Pearl River Estuary

Barium concentrations are significantly higher in the pore waters than in the corresponding bottom waters of the PRE (Figure 2), which potentially promotes a benthic flux of Ba into the overlying water column (Hong et al., 2018; Paytan & Kastner, 1996; Scholz et al., 2023). However, pore water $\delta^{138}Ba_{pw}$ signatures in the sediment surface are overall heavier than in the bottom waters above, in particular at station A03 in the middle PRE (Figure 4). These heavy pore water Ba isotopic signatures thus do not significantly impact the $\delta^{138}Ba$ signatures of the overlying bottom water, suggesting a small contribution from benthic inputs. In fact, we have recently demonstrated that $\delta^{138}Ba$ distributions in both the surface and bottom waters of the PRE are primarily controlled by water column processes that are particle adsorption-desorption at near-zero salinities followed by conservative mixing between low-salinity waters at the dissolved Ba concentration maximum and seawater (Cao et al., 2021).

Note that pore water imprints have been observed in the bottom waters of Kiel Bight (Germany), which are characterized by dissolved Ba concentrations and δ^{138}Ba signatures notably higher and lighter, respectively, than predicted values based on estuarine mixing calculations (Scholz et al., 2023). Such contrast might result from different water residence time of the two systems (Z. Zhang et al., 2020). Because of high river discharge and fast flow, the short residence time of bottom waters in the PRE highly likely diminishes the signal of benthic inputs (or the signal is difficult to be captured by current sampling and analyzing methods), which is opposite to the scenario in the relatively restricted Kiel Bight. This requires future studies of other estuaries under various hydrological conditions.

To further confirm the minor influence of benthic fluxes in the PRE, we use field-measured data of the bottom water at station A03 (salinity, Ba concentration, and δ^{138}Ba are 21.2, 149.8 nmol kg^{-1}, and +0.2‰, respectively) to carry out a simple mass balance calculation of Ba isotopic compositions. A two-endmember conservative mixing between the bottom water at station P06 showing the highest Ba concentrations in the PRE and the surface seawater of the South China Sea (Cao et al., 2021) predicts a theoretical water parcel at station A03 (salinity, Ba concentration, and δ^{138}Ba are 21.7, 120.4 nmol kg^{-1}, and +0.2‰, respectively), which has lower dissolved Ba concentrations than the field measurement. Assuming that the topmost pore water of this station (salinity, Ba concentration, and δ^{138}Ba$_{pw}$ are 22.2, 220.7 nmol kg^{-1}, and +0.7‰, respectively) is a third endmember of Ba to the overlying water column, its fraction in the A03 bottom water is estimated to be ∼30%, while the rest is contributed by the theoretical water parcel. In this case, the δ^{138}Ba signature of the A03 bottom water is predicted to be +0.4‰, which is markedly heavier than the field measurement of +0.2‰. Such disagreement between predictions and measurements of Ba isotope values indicates that the assumption is not valid. Consistency can only be reached when the δ^{138}Ba$_{pw}$ of the pore water source is lowered to +0.2‰, which is indistinguishable from that of the expected two-endmember mixture in the water column. This first order estimate thus suggests that direct "injection" of the heavy δ^{138}Ba$_{pw}$ from the topmost pore waters into the overlying water column rarely occurred during the sampling period in the PRE.

5. Conclusions

Pore water profiles of δ^{138}Ba$_{pw}$ in the PRE display significant and systematic variations primarily owing to Ba isotope fractionation during early diagenesis associated with processes within different sediment redox zones and depths of reaction fronts. Light δ^{138}Ba$_{pw}$ signatures correspond to high Ba concentrations in the pore waters and generally increase significantly during upward diffusion, likely mainly due to preferential removal of low-mass Ba isotopes into the solid phase. The overall consistent distributions of Ba and Mn concentrations in both the pore waters and the solid phase suggest that Mn oxides are the major non-detrital excess Ba carrier, while barite probably only plays a subordinate role given that similar δ^{138}Ba$_{pw}$ distributions correspond to variable barite saturation states between the study sites. Nevertheless, a diffusion-reaction model predicts that processes including the adsorption of Ba onto Mn (oxyhydr)oxides and precipitation of authigenic barite induce combined fractionation factors ($^{138}\varepsilon$) of -0.60 ± 0.10‰, which are comparable to those obtained by laboratory experiments or field measurements. This fractionation observed in the pore waters of the PRE needs verification in other estuarine systems and pelagic sediments, in particular via combined measurements of δ^{138}Ba in both pore waters and authigenic solid phases.

Data Availability Statement

Our data are archived at Cao et al. (2023).

References

Bates, S. L., Hendry, K. R., Pryer, H. V., Kinsley, C. W., Pyle, K. M., Woodward, E. M. S., & Horner, T. J. (2017). Barium isotopes reveal role of ocean circulation on barium cycling in the Atlantic. *Geochimica et Cosmochimica Acta*, *204*, 286–299. https://doi.org/10.1016/j.gca.2017.01.043

Berg, P., Risgaard-Petersen, N., & Rysgaard, R. (1998). Interpretation of measured concentration profiles in sediment pore water. *Limnology & Oceanography*, *43*(7), 1500–1510. https://doi.org/10.4319/lo.1998.43.7.1500

Böttcher, M. E., Geprägs, P., Neubert, N., von Allmen, K., Pretet, C., Samankassou, E., & Nägler, T. F. (2012). Barium isotope fractionation during experimental formation of the double carbonate BaMn[CO₃]₂ at ambient temperature. *Isotopes in Environmental and Health Studies*, *48*(3), 457–463. https://doi.org/10.1080/10256016.2012.673489

Böttcher, M. E., Neubert, N., von Allmen, K., Samankassou, E., & Nägler, T. F. (2018). Barium isotope fractionation during the experimental transformation of aragonite to witherite and of gypsum to barite, and the effect of ion (de)solvation. *Isotopes in Environmental and Health Studies*, *54*(3), 324–335. https://doi.org/10.1080/10256016.2018.1430692

Boudreau, P. (1997). *Diagenetic models and their implementation: Modelling transport and reactions in aquatic sediments*. Springer.

Bourg, I. C., Richter, F. M., Christensen, J. N., & Sposito, G. (2010). Isotopic mass dependence of metal cation diffusion coefficients in liquid water. *Geochimica et Cosmochimica Acta*, *74*(8), 2249–2256. https://doi.org/10.1016/j.gca.2010.01.024

Bridgestock, L., Hsieh, Y.-T., Porcelli, D., & Henderson, G. M. (2019). Increased export production during recovery from the Paleocene-Eocene thermal maximum constrained by sedimentary Ba isotopes. *Earth and Planetary Science Letters*, *510*, 53–63. https://doi.org/10.1016/j.epsl.2018.12.036

Bridgestock, L., Hsieh, Y.-T., Porcelli, D., Homoky, W. B., Bryan, A., & Henderson, G. M. (2018). Controls on the barium isotope compositions of marine sediments. *Earth and Planetary Science Letters*, *481*, 101–110. https://doi.org/10.1016/j.epsl.2017.10.019

Bridgestock, L., Nathan, J., Paver, R., Hsieh, Y.-T., Porcelli, D., Tanzil, J., et al. (2021). Estuarine processes modify the isotope composition of dissolved riverine barium fluxes to the ocean. *Chemical Geology*, *579*, 120340. https://doi.org/10.1016/j.chemgeo.2021.120340

Cai, P., Shi, X., Hong, Q., Li, Q., Liu, L., Guo, X., & Dai, M. (2015). Using ^{224}Ra/^{228}Th disequilibrium to quantify benthic fluxes of dissolved inorganic carbon and nutrients into the Pearl River Estuary. *Geochimica et Cosmochimica Acta*, *170*, 188–203. https://doi.org/10.1016/j.gca.2015.08.015

Cao, Z., Li, Y., Rao, X., Yu, Y., Hathorne, E. C., Siebert, C., et al. (2020). Constraining barium isotope fractionation in the upper water column of the South China Sea. *Geochimica et Cosmochimica Acta*, *288*, 120–137. https://doi.org/10.1016/j.gca.2020.08.008

Cao, Z., Rao, X., Li, Y., & Hong, Q. (2023). A dataset of stable barium isotopes in pore waters and sediments of the Pearl River Estuary (Version V1) [Dataset]. Science Data Bank. https://doi.org/10.57760/sciencedb.08297

Cao, Z., Rao, X., Yu, Y., Siebert, C., Hathorne, E. C., Liu, B., et al. (2021). Stable barium isotope dynamics during estuarine mixing. *Geophysical Research Letters*, *48*(19), e2021GL095680. https://doi.org/10.1029/2021gl095680

Cao, Z., Siebert, C., Hathorne, E. C., Dai, M., & Frank, M. (2016). Constraining the oceanic barium cycle with stable barium isotopes. *Earth and Planetary Science Letters*, *434*, 1–9. https://doi.org/10.1016/j.epsl.2015.11.017

Cao, Z., Siebert, C., Hathorne, E. C., Dai, M., & Frank, M. (2020). Corrigendum to "Constraining the oceanic barium cycle with stable barium isotopes". *Earth and Planetary Science Letters*, *530*, 116003. https://doi.org/10.1016/j.epsl.2019.116003

Charbonnier, Q., Bouchez, J., Gaillardet, J., & Gayer, É. (2020). Barium stable isotopes as a fingerprint of biological cycling in the Amazon River basin. *Biogeosciences*, *17*(23), 5989–6015. https://doi.org/10.5194/bg-17-5989-2020

Charette, M. A., Sholkovitz, E. R., & Hansell, C. M. (2005). Trace element cycling in a subterranean estuary: Part 1. Geochemistry of the permeable sediments. *Geochimica et Cosmochimica Acta*, *69*(8), 2095–2109. https://doi.org/10.1016/j.gca.2004.10.024

Colbert, D., & McManus, J. (2005). Importance of seasonal variability and coastal processes on estuarine manganese and barium cycling in a Pacific Northwest estuary. *Continental Shelf Research*, *25*(11), 1395–1414. https://doi.org/10.1016/j.csr.2005.02.003

Crockford, P. W., Wing, B. A., Paytan, A., Hodgskiss, M. S., Mayfield, K. K., Hayles, J. A., et al. (2019). Barium-isotopic constraints on the origin of post-Marinoan barites. *Earth and Planetary Science Letters*, *519*, 234–244. https://doi.org/10.1016/j.epsl.2019.05.018

Dai, M., Guo, X., Zhai, W., Yuan, L., Wang, B., Wang, L., et al. (2006). Oxygen depletion in the upper reach of the Pearl River Estuary during a winter drought. *Marine Chemistry*, *102*(1–2), 159–169. https://doi.org/10.1016/j.marchem.2005.09.020

Edmond, J. M., Spivack, A., Grant, B. C., Hu, M.-H., Chen, Z., Chen, S., & Zeng, X. (1985). Chemical dynamics of the Changjiang estuary. *Continental Shelf Research*, *4*(1–2), 17–36. https://doi.org/10.1016/0278-4343(85)90019-6

Geyman, B. M., Ptacek, J. L., LaVigne, M., & Horner, T. J. (2019). Barium in deep-sea bamboo corals: Phase associations, barium stable isotopes, & prospects for paleoceanography. *Earth and Planetary Science Letters*, *525*, 115751. https://doi.org/10.1016/j.epsl.2019.115751

Gingele, F. X., Zabel, M., Kasten, S., Bonn, W. J., & Nürnberg, C. C. (1999). Biogenic barium as a proxy for paleoproductivity: Methods and limitations of application. In G. Fischer & G. Wefer (Eds.), *Use of proxies in paleoceanography: Examples from the South Atlantic* (pp. 345–364). Springer.

Gong, Y., Zeng, Z., Zhou, C., Nan, X., Yu, H., Lu, Y., et al. (2019). Barium isotopic fractionation in latosol developed from strongly weathered basalt. *Science of the Total Environment*, *687*, 1295–1304. https://doi.org/10.1016/j.scitotenv.2019.05.427

Gou, L.-F., Jin, Z., Galy, A., Gong, Y.-Z., Nan, X.-Y., Jin, C., et al. (2020). Seasonal riverine barium isotopic variation in the middle Yellow River: Sources and fractionation. *Earth and Planetary Science Letters*, *531*, 115990. https://doi.org/10.1016/j.epsl.2019.115990

Haese, R. R., Hensen, C., & de Lange, G. J. (2006). Pore water geochemistry of eastern Mediterranean mud volcanoes: Implications for fluid transport and fluid origin. *Marine Geology*, *225*(1–4), 191–208. https://doi.org/10.1016/j.margeo.2005.09.001

He, B., Dai, M., Huang, W., Liu, Q., Chen, H., & Xu, L. (2010). Sources and accumulation of organic carbon in the Pearl River Estuary surface sediment as indicated by elemental, stable carbon isotopic, and carbohydrate compositions. *Biogeosciences*, *7*(10), 3343–3362. https://doi.org/10.5194/bg-7-3343-2010

He, B., Dai, M., Zhai, W., Guo, X., & Wang, L. (2014). Hypoxia in the upper reaches of the Pearl River Estuary and its maintenance mechanisms: A synthesis based on multiple year observations during 2000-2008. *Marine Chemistry*, *167*, 13–24. https://doi.org/10.1016/j.marchem.2014.07.003

Hemsing, F., Hsieh, Y.-T., Bridgestock, L., Spooner, P. T., Robinson, L. F., Frank, N., & Henderson, G. M. (2018). Barium isotopes in cold-water corals. *Earth and Planetary Science Letters*, *491*, 183–192. https://doi.org/10.1016/j.epsl.2018.03.040

Henkel, S., Kasten, S., Hartmann, J. F., Busso, A. S., & Staubwasser, M. (2018). Iron cycling and stable Fe isotope fractionation in Antarctic shelf sediments, King George Island. *Geochimica et Cosmochimica Acta*, *237*, 320–338. https://doi.org/10.1016/j.gca.2018.06.042

Henkel, S., Kasten, S., Poulton, S. W., & Staubwasser, M. (2016). Determination of the stable iron isotope composition of sequentially leached iron phases in marine sediments. *Chemical Geology*, *421*, 93–102. https://doi.org/10.1016/j.chemgeo.2015.12.003

Henkel, S., Mogollón, J. M., Nöthen, K., Franke, C., Bogus, K., Robin, E., et al. (2012). Diagenetic barium cycling in Black Sea sediments—A case study for anoxic marine environments. *Geochimica et Cosmochimica Acta*, *88*, 88–105. https://doi.org/10.1016/j.gca.2012.04.021

Hong, Q., Cai, P., Geibert, W., Cao, Z., Stimac, I., Liu, L., & Li, Q. (2018). Benthic fluxes of metals into the Pearl River Estuary based on ^{224}Ra/^{228}Th disequilibrium: From alkaline Earth elements (Ba) to redox sensitive metals (U, Mn, and Fe). *Geochimica et Cosmochimica Acta*, *237*, 223–239. https://doi.org/10.1016/j.gca.2018.06.036

Horner, T. J., Kinsley, C. W., & Nielsen, S. G. (2015). Barium-isotopic fractionation in seawater mediated by barite cycling and ocean circulation. *Earth and Planetary Science Letters*, *430*, 511–522. https://doi.org/10.1016/j.epsl.2015.07.027

Horner, T. J., Pryer, H. V., Nielsen, S. G., Crockford, P. W., Gauglitz, J. M., Wing, B. A., & Ricketts, R. D. (2017). Pelagic barite precipitation at micromolar ambient sulfate. *Nature Communications*, *8*(1), 1242. https://doi.org/10.1038/s41467-017-01229-5

Hsieh, Y.-T., & Henderson, G. M. (2017). Barium stable isotopes in the global ocean: Tracer of Ba inputs and utilization. *Earth and Planetary Science Letters*, *473*, 269–278. https://doi.org/10.1016/j.epsl.2017.06.024

Iversen, N., & Jørgensen, B. B. (1993). Diffusion coefficients of sulfate and methane in marine sediments: Influence of porosity. *Geochimica et Cosmochimica Acta*, *57*(3), 571–578. https://doi.org/10.1016/0016-7037(93)90368-7

Joung, D., & Shiller, A. M. (2014). Dissolved barium behavior in Louisiana Shelf waters affected by the Mississippi/Atchafalaya River mixing zone. *Geochimica et Cosmochimica Acta*, *141*, 303–313. https://doi.org/10.1016/j.gca.2014.06.021

Kasten, S., Zabel, M., Heuer, V., & Hensen, C. (2003). Processes and signals of nonsteady-state diagenesis in deep-sea sediments and their pore waters. In G. Wefer, S. Mulitza, & V. Ratmeyer (Eds.), *The South Atlantic in the late quaternary: Reconstruction of material budgets and current systems* (pp. 431–459). Springer-Verlag.

Li, D., Gan, J., Hui, R., Liu, Z., Yu, L., Lu, Z., & Dai, M. (2020). Vortex and biogeochemical dynamics for the hypoxia formation within the coastal transition zone off the Pearl River Estuary. *Journal of Geophysical Research: Oceans*, *125*(8), e2020JC016178. https://doi.org/10.1029/2020jc016178

Mavromatis, V., van Zuilen, K., Purgstaller, B., Baldermann, A., Nägler, T. F., & Dietzel, M. (2016). Barium isotope fractionation during witherite ($BaCO_3$) dissolution, precipitation and at equilibrium. *Geochimica et Cosmochimica Acta*, *190*, 72–84. https://doi.org/10.1016/j.gca.2016.06.024

McManus, J., Berelson, W. M., Klinkhammer, G. P., Johnson, K. S., Coale, K. H., Anderson, R. F., et al. (1998). Geochemistry of barium in marine sediments: Implications for its use as a paleoproxy. *Geochimica et Cosmochimica Acta*, *62*(21–22), 3453–3473. https://doi.org/10.1016/s0016-7037(98)00248-8

Monnin, C. (1999). A thermodynamic model for the solubility of barite and celestite in electrolyte solutions and seawater from 0 to 200°C and to 1 kbar. *Chemical Geology*, *153*(1–4), 187–209. https://doi.org/10.1016/s0009-2541(98)00171-5

Moore, W. S., & Shaw, T. J. (2008). Fluxes and behavior of radium isotopes, barium, and uranium in seven Southeastern US rivers and estuaries. *Marine Chemistry*, *108*(3–4), 236–254. https://doi.org/10.1016/j.marchem.2007.03.004

Nan, X., Yu, H.-M., Rudnick, R. L., Gasching, R. M., Xu, J., Li, W.-Y., et al. (2018). Barium isotopic composition of the upper continental crust. *Geochimica et Cosmochimica Acta*, *233*, 33–49. https://doi.org/10.1016/j.gca.2018.05.004

Nielsen, S. G., Horner, T. J., Pryer, H. V., Blusztajn, J., Shu, Y., Kurz, M. D., & Le Roux, V. (2018). Barium isotope evidence for pervasive sediment recycling in the upper mantle. *Science Advances*, *4*(7), eaas8675. https://doi.org/10.1126/sciadv.aas8675

Oni, O., Miyatake, T., Kasten, S., Richter-Heitmann, T., Fischer, D., Wagenknecht, L., et al. (2015). Distinct microbial populations are tightly linked to the profile of dissolved iron in the methanic sediments of the Helgoland mud area, North Sea. *Frontiers in Microbiology*, *6*. https://doi.org/10.3389/fmicb.2015.00365

Paytan, A., & Kastner, M. (1996). Benthic Ba fluxes in the central Equatorial Pacific, implications for the oceanic Ba cycle. *Earth and Planetary Science Letters*, *142*(3–4), 439–450. https://doi.org/10.1016/0012-821x(96)00120-3

Plewa, K., Meggers, H., & Kasten, S. (2006). Barium in sediments off northwest Africa: A tracer for paleoproductivity or meltwater events? *Paleoceanography*, *21*(2), PA2015. https://doi.org/10.1029/2005PA001136

Qian, W., Gan, J., Liu, J., He, B., Lu, Z., Guo, X., et al. (2018). Current status of emerging hypoxia in a eutrophic estuary: The lower reach of Pearl River Estuary, China. *Estuarine, Coastal and Shelf Science*, *205*, 58–67. https://doi.org/10.1016/j.ecss.2018.03.004

Rabouille, C., Conley, D. J., Dai, M., Cai, W.-J., Chen, C.-T. A., Lansard, B., et al. (2008). Comparison of hypoxia among four river-dominated ocean margins: The Changjiang (Yangtze), Mississippi, Pearl and Rhone rivers. *Continental Shelf Research*, *28*(12), 1527–1537. https://doi.org/10.1016/j.csr.2008.01.020

Reitz, A., Pfeifer, K., de Lange, G. J., & Klump, J. (2004). Biogenic barium and the detrital Ba/Al ratio: A comparison of their direct and indirect determination. *Marine Geology*, *204*(3–4), 289–300. https://doi.org/10.1016/s0025-3227(04)00004-0

Riedinger, N., Kasten, S., Gröger, J., Franke, C., & Pfeifer, K. (2006). Active and buried authigenic barite fronts in sediments from the eastern Cape Basin. *Earth and Planetary Science Letters*, *241*(3–4), 876–888. https://doi.org/10.1016/j.epsl.2005.10.032

Rudnick, R. L., & Gao, S. (2014). Composition of the continental crust. In H. D. Holland & K. K. Turekian (Eds.), *Treatise on geochemistry* (2nd ed., Vol. 4, pp. 1–51). Elsevier.

Rushdi, A. I., McManus, J., & Collier, R. W. (2000). Marine barite and celestite saturation in seawater. *Marine Chemistry*, *69*(1–2), 19–31. https://doi.org/10.1016/s0304-4203(99)00089-4

Schenau, S. J., Prins, M. A., De Lange, G. J., & Monnin, C. (2001). Barium accumulation in the Arabian Sea: Controls on barite preservation in marine sediments. *Geochimica et Cosmochimica Acta*, *65*(10), 1545–1556. https://doi.org/10.1016/s0016-7037(01)00547-6

Schnakenberg, A., Aromokeye, D. A., Kulkarni, A., Maier, L., Wunder, L. C., Richter-Heitmann, T., et al. (2021). Electron acceptor availability shapes anaerobically methane oxidizing archaea (ANME) communities in South Georgia sediments. *Frontiers in Microbiology*, *12*. https://doi.org/10.3389/fmicb.2021.617280

Scholz, F., Cheng, J., Zhang, Z., Vosteen, P., Siebert, C., & Frank, M. (2023). Benthic-pelagic coupling and isotopic fractionation of barium in Kiel Bight, SW Baltic Sea. *Frontiers in Marine Science*, *10*. https://doi.org/10.3389/fmars.2023.1101095

Seeberg-Elverfeldt, J., Schlüter, M., Feseker, T., & Kölling, M. (2005). Rhizon sampling of pore waters near the sediment/water interface of aquatic systems. *Limnology and Oceanography: Methods*, *3*(8), 361–371. https://doi.org/10.4319/lom.2005.3.361

Su, J., Dai, M., He, B., Wang, L., Gan, J., Guo, X., et al. (2017). Tracing the origin of the oxygen-consuming organic matter in the hypoxic zone in a large eutrophic estuary: The lower reach of the Pearl River Estuary, China. *Biogeosciences*, *14*(18), 4085–4099. https://doi.org/10.5194/bg-14-4085-2017

Taylor, S. R., & McLennan, S. M. (1985). *The continental crust: Its composition and evolution*. Blackwell Scientific Publications, (pp. 312).

Torres, M. E., Bohrmann, G., & Suess, E. (1996). Authigenic barites and fluxes of barium associated with fluid seeps in the Peru subduction zone. *Earth and Planetary Science Letters*, *144*(3–4), 469–481. https://doi.org/10.1016/s0012-821x(96)00163-x

van Zuilen, K., Müller, T., Nägler, T. F., Dietzel, M., & Küsters, T. (2016). Experimental determination of barium isotope fractionation during diffusion and adsorption processes at low temperatures. *Geochimica et Cosmochimica Acta*, *186*, 226–241. https://doi.org/10.1016/j.gca.2016.04.049

van Zuilen, K., Nägler, T. F., & Bullen, T. D. (2016). Barium isotopic compositions of geological reference materials. *Geostandards and Geoanalytical Research*. https://doi.org/10.1111/ggr.12122

von Allmen, K., Böttcher, M. E., Samankassou, E., & Nägler, T. F. (2010). Barium isotope fractionation in the global barium cycle: First evidence from barium minerals and precipitation experiments. *Chemical Geology*, *277*(1–2), 70–77. https://doi.org/10.1016/j.chemgeo.2010.07.011

Vosteen, P., Spiegel, T., Gledhill, M., Frank, M., Zabel, M., & Scholz, F. (2022). The fate of sedimentary reactive iron at the land-ocean interface: A case study from the Amazon shelf. *Geochemistry, Geophysics, Geosystems*, *23*(11), e2022GC010543. https://doi.org/10.1029/2022gc010543

Wunder, L. C., Aromokeye, D. A., Yin, X., Richter-Heitmann, T., Willis-Poratti, G., Schnakenberg, A., et al. (2021). Iron and sulfate reduction structure microbial communities in (sub-)Antarctic sediments. *ISME Journal*, *15*(12), 3587–3604. https://doi.org/10.1038/s41396-021-01014-9

Yu, Y., Siebert, C., Fietzke, J., Goepfert, T., Hathorne, E. C., Cao, Z., & Frank, M. (2020). The impact of MC-ICP-MS plasma conditions on the accuracy and precision of stable isotope measurements evaluated for barium isotopes. *Chemical Geology*, *549*, 119697. https://doi.org/10.1016/j.chemgeo.2020.119697

Yu, Y., Xie, R. C., Gutjahr, M., Laukert, G., Cao, Z., Hathorne, E., et al. (2022). High latitude controls on dissolved barium isotope distributions in the global ocean. *Geochemical Perspectives Letters*, *24*, 22–26. https://doi.org/10.7185/geochemlet.2242

Zhang, L., Wang, L., Yin, K., Lü, Y., Zhang, D., Yang, Y., & Huang, X. (2013). Pore water nutrient characteristics and the fluxes across the sediment in the Pearl River estuary and adjacent waters, China. *Estuarine, Coastal and Shelf Science*, *133*, 182–192. https://doi.org/10.1016/j.ecss.2013.08.028

Zhang, W., Zheng, J., Ji, X., Hoitink, A. J. F., van der Vegt, M., & Zhu, Y. (2013). Surficial sediment distribution and the associated net sediment transport pattern in the Pearl River Estuary, South China. *Continental Shelf Research*, *61–62*, 41–51. https://doi.org/10.1016/j.csr.2013.04.011

Zhang, Z., Cao, Z., Grasse, P., Dai, M., Gao, L., Kuhnert, H., et al. (2020). Dissolved silicon isotope dynamics in large river estuaries. *Geochimica et Cosmochimica Acta*, *273*, 367–382. https://doi.org/10.1016/j.gca.2020.01.028

Zhao, Y., Uthaipan, K., Lu, Z., Li, Y., Liu, J., Liu, H., et al. (2021). Destruction and reinstatement of coastal hypoxia in the South China Sea off the Pearl River estuary. *Biogeosciences*, *18*(8), 2755–2775. https://doi.org/10.5194/bg-18-2755-2021